

# Experimental investigation of the fatigue crack growth behavior in wire arc additively manufactured ER100S-1 steel specimens

Anna Ermakova<sup>1</sup> | Supriyo Ganguly<sup>2</sup> | Javad Razavi<sup>3</sup> | Filippo Berto<sup>3</sup> | Ali Mehmanparast<sup>1</sup>

<sup>1</sup>Offshore Renewable Energy Engineering Centre, Cranfield University, Cranfield, UK

<sup>2</sup>Welding Engineering and Laser Processing Centre, Cranfield University, Cranfield, UK

<sup>3</sup>Department of Mechanical and Industrial Engineering, Norwegian University of Science and Technology (NTNU), Trondheim, Norway

## Correspondence

Ali Mehmanparast, Offshore Renewable Energy Engineering Centre, Cranfield University, Cranfield MK43 0AL, UK.  
Email: a.mehmanparast@cranfield.ac.uk

## Funding information

UK Engineering and Physical Sciences Research Council, Grant/Award Number: L016303

## Abstract

Wire arc additive manufacturing (WAAM) is an advanced fabrication technology for the rapid and efficient production of large-scale engineering structures. In order to design WAAM components for a given loading condition, it is essential to characterize the mechanical and failure behavior of the parts. In this study, the performance of ER100S-1 low carbon steel has been investigated by performing fatigue crack growth tests on compact tension specimens extracted from a WAAM built wall. The experimental results have been compared with the recommended trends in the BS7910 standard and with data available in the literature. Metallurgical investigations have been carried out to explore the microstructural effects on the fatigue behavior of the WAAM built components. The specimen location and orientation effects were comprehensively examined, and the results are discussed in terms of the influence of macroscopic and microscopic deformation on the overall response of the WAAM built components under fatigue loading conditions.

## KEYWORDS

additive materials, fatigue crack growth, structural integrity

## 1 | INTRODUCTION

Additive manufacturing (AM) technology is a layer-by-layer manufacturing technique that enables the fabrication of complex shapes in a continuous production process without an expensive conventional set-up and tools. The AM technology is rapidly evolving from simple prototyping to fabrication and repairing of critical large-scale industrial parts.<sup>1–3</sup> The AM components generally do not show isotropic behavior due to the layer-wise nature of the AM process and continuous melting and

solidification of the material, which induces residual stresses and microstructural changes. Depending on the AM process conditions, the parts may have a high likelihood of porosity and internal defects which would subsequently influence the mechanical response and failure behavior of the AM parts.

Wire arc additive manufacturing (WAAM) is a direct energy deposition technique that combines an electric arc as a heat source and a wire as feedstock and provides the highest deposition rates among all AM techniques,<sup>4</sup> which makes it suitable for the production of large-scale

This is an open access article under the terms of the Creative Commons Attribution License, which permits use, distribution and reproduction in any medium, provided the original work is properly cited.

© 2021 The Authors. *Fatigue & Fracture of Engineering Materials & Structures* published by John Wiley & Sons Ltd.

structures. Moreover, compared to the powder-based AM techniques, using wire as a feedstock reduces the level of safety-related risks in the course of the manufacturing process. The WAAM technique can be utilized for the fabrication of simple and complex parts by employing a wide range of alloys such as aluminum, steels and titanium, and functionally graded materials.<sup>5</sup> In addition to the fabrication of new parts, the WAAM technique also facilitates the repair of damaged structures, as an alternative to the replacement of the entire component.<sup>6,7</sup> Similarly to all AM techniques, as well as all the advantages mentioned for WAAM, this technique may also involve some disadvantages. The main disadvantage of such a fabrication method is the possibility of relatively high roughness on the outer surface of the as-built parts and dimensional inaccuracies that may impose the requirement of further post-deposition treatments such as surface machining, high pressure rolling, etc. The WAAM technique has been developed and investigated since the 1990s and is currently adopted by several industries such as aerospace and automotive for the fabrication of industrial-scale components.<sup>8,9</sup> Further developments have been carried out in recent years to increase the scale of the WAAM built parts from component size to the structural level by printing a large-scale bridge.<sup>10</sup> In order to explore the suitability of the WAAM technique for low-cost fabrication of large-scale structures, the WAAM built parts made of conventional steels (i.e., which are relatively cheap) must be fully characterized under various loading conditions and in different environments.

For industrial applications where the engineering component or structure is subjected to repetitive load cycles during service, such as marine structures, fatigue assessment is a critical consideration at the design and life assessment stages.<sup>11–13</sup> Particularly for life prediction purposes, it is crucial to investigate the fatigue behavior of the material to better understand the damage evolution and failure behavior in such components. Therefore, feasibility studies must be performed on the fatigue behavior of WAAM built components made of various alloys to examine the suitability of the WAAM technique and particular alloys for consideration in industrial applications where the component or structure is subjected to repeated cyclic stresses. While there are some limited fatigue crack growth (FCG) data available in the literature on WAAM built parts made of titanium<sup>14,15</sup> and occasionally stainless steel,<sup>16,17</sup> the fatigue response of more effective low carbon steels is yet to be explored for application in less safety-critical industries such as offshore wind. Knowing that steel alloys are the most common types of material utilized in the fabrication of metallic structures in offshore applications, further research into the FCG behavior of WAAM built parts

made of steel alloys would rapidly expand the extent of application of this efficient AM technology and enable this technology to be considered for low-cost fabrication of offshore renewable energy structures.

The fatigue crack propagation behavior of WAAM built parts using titanium Ti-6Al-4V alloy was examined by Zhang et al.,<sup>18</sup> where compact tension, C(T), specimens were extracted from WAAM walls. The specimens had different orientations with the crack initiation region in substrate or the WAAM built area. The maximum load, load ratio, and frequency in these tests were 5 kN, 0.1, and 10 Hz, respectively. It was reported that the crack propagated along straight and smooth lines in the wrought part of the specimen and in tortuous paths in the WAAM built region, due to different microstructural characteristics and lamellar structure of the WAAM part. Furthermore, lower crack propagation rates were observed in the WAAM specimens compared to the wrought substrate. Similar observations were reported by the same authors in further analysis of such C(T) specimens.<sup>19</sup> Gordon et al.<sup>20</sup> examined the fatigue behavior of WAAM built parts using 304 L stainless steel by performing fatigue tests on single edge notched bend, SEN(B), thin specimens extracted from different wall locations and in two different orientations with respect to the building direction. The experiments were conducted at a constant load range of 0.7 kN, load ratio of 0.1, and frequency of 10 Hz. The results show that as-printed WAAM specimens have improved the FCG resistance compared to the conventional wrought 304 L stainless steel. In addition, it was observed that the vertical WAAM specimens displayed lower fatigue propagation rates compared to the horizontal specimens, which can be due to the long columnar grains and strong texture in the WAAM built direction. A set of WAAM built Ti-6Al-4V titanium alloy specimens were tested under fatigue loading conditions by Zhang et al.<sup>14,21</sup> Thicker C(T) specimens were also extracted with two different crack orientations with respect to the WAAM deposited layers. The FCG rates in WAAM specimens were found to be lower than the wrought counterpart. Moreover, the crack growth rate was found to be lower in specimens with the propagating path across the AM layers, compared to those where the crack was growing along the layers. These findings suggest that the WAAM process can be considered as an alternative technology for manufacturing purposes.

The experimental results reported in previous studies have shown that the FCG behavior of the WAAM built parts strongly depend on the material and crack orientation. In this study, the FCG behavior of WAAM built parts made of ER100S-1 steel has been investigated to explore the suitability of this material for the WAAM

production of offshore structures which are subjected to cyclic loading conditions. Also included in this study is a sensitivity analysis of the specimen orientation and extraction location, with respect to the WAAM built wall, on the fatigue performance of the extracted specimens. Details of the manufacturing process of the WAAM walls, specimen extraction plan and geometry, the test set-up and data analysis procedure, and obtained test results are presented below. The results have been discussed in terms of the material microstructure effects on the cracking behavior of ER100S-1 WAAM built parts. Furthermore, the same results have been compared with the recommended FCG trends available in standards and also the existing test data on wrought steels in order to critically assess the fatigue performance of WAAM built parts compared to conventional welded structures.

## 2 | MANUFACTURING SET-UP AND SPECIMEN EXTRACTION

A high strength metal wire ER100S-1 with low carbon and high manganese was used in this study. This material is normally used for shielded arc welding on a variety of steels employed in critical applications, such as mining, pressure vessels, shipbuilding, military equipment, and high strength products. The yield stress of ER100S-1 is equal to or greater than 690 MPa with the ultimate tensile strength (UTS) of 760 MPa.<sup>22</sup> This material offers excellent toughness; however, its mechanical properties significantly depend on the level of preheating, interpass temperature, and post-weld heat treatment. A spool of Böhler Welding ER100S-1 wire<sup>23</sup> was used in this study with the chemical composition listed in Table 1.

A Cold Metal Transfer (CMT)-based WAAM process, with the manufacturing parameters summarized in Table 2, was used to produce an additively manufactured wall for this study. The WAAM set-up consists of the CMT power source, and a robot arm with the torch that feeds the wire and supplies shielding gas simultaneously. An exhaust fan draws off the generated fumes and heat in the course of the WAAM process. The manufacturing set-up and completed wall are shown in Figure 1A. The WAAM deposition process was started in the middle of the base plate which was cut from EN10025 rolled structural steel with dimensions of  $420 \times 200 \times 12$  mm<sup>3</sup>. Each side of the base plate was fixed onto the working table with two clamps to prevent any bending and movement due to the thermal energy input. Once the fabrication of the WAAM wall was completed and the part was cooled down to the ambient temperature, the clamps were removed. The additive layers in the WAAM wall were deposited on top of each other in an oscillating manner<sup>24</sup>

TABLE 1 Chemical composition of ER100S-1 material (wt.-%)<sup>23</sup>

	C	Mn	Cr	Si	Ni	Mo
ER100S-1	0.08	1.70	0.20	0.60	1.50	0.50

TABLE 2 CMT-WAAM fabrication parameters

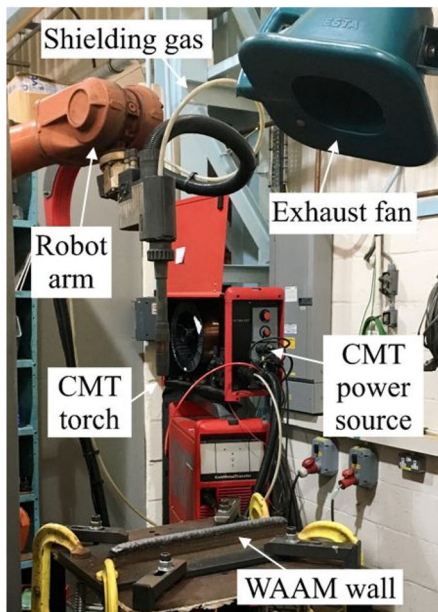
Shielding gas	Ar + 20% CO <sub>2</sub>
Gas flow rate	15 L/min
Wire diameter	1.2 mm
Wire feed speed	7.5 m/min
Robot traveling speed	7.33 mm/s
Dwell time	120 s

in order to create a relatively thick wall with approximately 355 mm length ( $X$  direction in Figure 1B), 24 mm thickness ( $Y$  direction), and 140 mm height ( $Z$  direction).

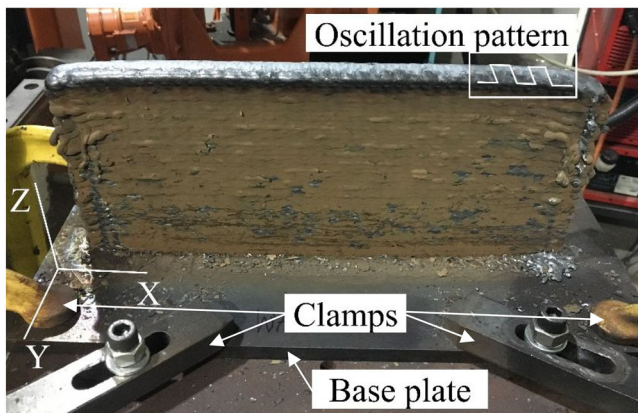
Upon completion of the WAAM wall fabrication, eight stepped notched C(T) specimens were extracted using the Electrical Discharge Machining (EDM) technique. Four of the specimens were extracted from the bottom of the wall (near the base plate) and four from the top of the WAAM wall. As shown in Figure 1C, specimens denoted CT-T-1 to CT-T-4 were located at the top of the wall, whereas CT-B-1 to CT-B-4 were from the bottom. Moreover, the specimens were extracted with two different crack orientations; half of them had vertical (V) orientation—with the crack plane perpendicular to the deposition direction (for example, CT-T-1 or CT-B-1), and the other half had horizontal (H) orientation—with the crack plane parallel to the AM layers (for example, CT-T-4 or CT-B-2). The geometry of C(T) specimens was selected in accordance with the ASTM E647<sup>25</sup> standard with the width of  $W = 50$  mm, height of  $H = 60$  mm, total thickness of  $B = 16$  mm, and the initial crack length  $a_0 = 17$  mm (before pre-fatigue cracking). Knife edges were machined at the crack mouth of the C(T) specimens following the instructions provided in the E1820<sup>26</sup> standard in order to accommodate a clip gauge for crack growth monitoring using the compliance measurements throughout the tests.<sup>27</sup>

## 3 | FATIGUE CRACK GROWTH TEST SET-UP AND DATA ANALYSIS

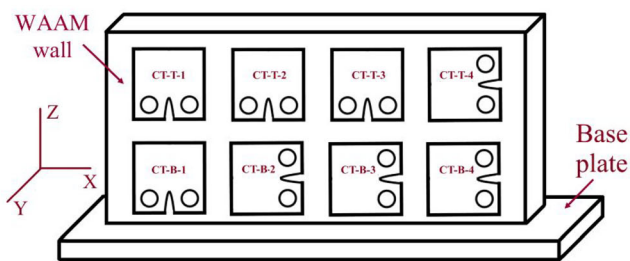
FCG tests were performed on a 100 kN servo-hydraulic Instron machine under Mode I fracture mechanics loading conditions according to the ASTM E647<sup>25</sup> standard. All tests were conducted in air at room temperature with



(A)



(B)



(C)

FIGURE 1 The fabrication process: (A) CMT WAAM set-up, (B) completed wall, and (C) schematic demonstration of the specimen extraction plan [Colour figure can be viewed at wileyonlinelibrary.com]

the load ratio (i.e., the ratio of minimum to maximum load  $P_{min}/P_{max}$ ) of  $R = 0.1$  and maximum applied load of  $P_{max} = 10$  kN. The fatigue cycles were introduced using a

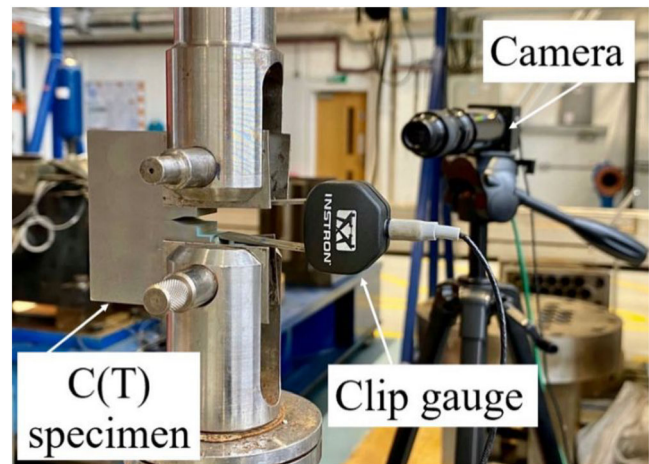


FIGURE 2 Fatigue crack growth test set-up [Colour figure can be viewed at wileyonlinelibrary.com]

constant amplitude sinusoidal cyclic waveform at 5 Hz frequency. Prior to FCG testing, all specimens were pre-fatigue cracked to approximately 20 mm ( $a_{i,p}/W = 0.4$ ) under fatigue loading conditions using the load decreasing approach, to introduce an infinitely sharp crack tip ahead of the machined notch. During the fatigue pre-cracking phase, it was ensured that the final value of maximum stress intensity factor  $K_{max}$  did not exceed the initial  $K_{max}$  in the actual FCG tests.

The instantaneous crack lengths,  $a_i$ , during the pre-cracking phase and FCG tests were estimated using the unloading compliance method, by attaching a clip gauge onto the knife edges located at the crack mouth of the specimens. Moreover, two high-resolution cameras were placed at the back and in front of the set-up to monitor the crack growth on each side of the specimen and capture the crack paths throughout the tests. The crack lengths were measured at the outer surfaces of the C(T) specimens using the cameras to validate the data obtained from the compliance method. All C(T) specimens were tested until the value of the crack length estimated by the compliance technique reached 35 mm ( $a_{f,c}/W = 0.7$ ). The fatigue test set-up and crack growth monitoring tools are demonstrated in Figure 2.

The number of cycles and the instantaneous crack lengths were continuously captured during the fatigue tests and the FCG rates,  $da/dN$ , were subsequently calculated using a combination of the secant method for the first and last three data points and the 7-point incremental polynomial method for the rest of the data points. The stress intensity factor (SIF) range,  $\Delta K$ , was obtained according to the shape function equation shown in Equation 1, developed by Mehmanparast et al.,<sup>28</sup> which provides accurate solutions of the shape function for a wider range of crack lengths,  $0.2 \leq a/W \leq 0.7$ , in a C(T)

specimen compared to that available in ASTM E647<sup>25</sup> which involves a relatively large percentage of error at shorter crack lengths. In Equation 1,  $\alpha$  is the normalized crack length  $a/W$ , and  $\Delta P$  is the load range which is defined as the difference between  $P_{max}$  and  $P_{min}$ .

$$\Delta K = \frac{\Delta P}{B\sqrt{W}} \cdot \frac{(2+\alpha)}{(1-\alpha)^{\frac{3}{2}}} \cdot \left( -372.12\alpha^6 + 1628.60\alpha^5 - 2107.46\alpha^4 + 1304.65\alpha^3 - 391.20\alpha^2 + 54.81\alpha + 7.57 \right). \quad (1)$$

## 4 | TEST RESULTS AND DISCUSSION

The recorded data during the FCG tests, which comprised the crack length  $a$  and the number of cycles  $N$ , are shown for each specimen and compared with each other in Figure 3. As seen in this figure, the initial crack length after fatigue pre-cracking was approximately 20 mm for all specimens, except for the CT-T-4 specimen which had a longer starting crack and therefore exhibited a shorter FCG test duration. The comparison of the crack growth trends in Figure 3 shows that the duration of the fatigue tests performed on specimens extracted from the top of the WAAM wall was on average approximately 3.9 times longer, compared to those extracted from the bottom of the wall. Moreover, it can be observed in Figure 3 that the FCG trends obtained from the bottom specimens are consistently similar, whilst the specimens extracted from the top of the wall exhibited some noticeable levels of

inconsistency in the FCG trends. The obtained FCG results in Figure 3 show that, for the material examined in this study the FCG test duration and trend strongly depend on the location at which the specimens were extracted from the ER100S-1 WAAM wall.

The FCG rate,  $da/dN$ , obtained from the tests on C(T) specimens was correlated with the SIF range,  $\Delta K$ , and the results are presented in Figure 4A. It can be seen in this figure that for the given loading condition, the FCG results on the specimens extracted from the bottom of the WAAM wall show a higher crack growth rate at the low and intermediate values of  $\Delta K$  compared to those extracted from the top of the wall. However, at larger values of  $\Delta K$ , the difference between the FCG rates in the bottom and top specimens decreases and eventually diminishes. The results in Figure 4A show that the FCG trends obtained from horizontally oriented specimens extracted from the bottom of the WAAM wall (CT-B-2, CT-B-3, and CT-B-4) fall upon each other indicating a good repeatability in those tests from horizontal specimens while the vertically oriented specimen from the bottom of the wall (CT-B-1) initially followed the same trend as the horizontal specimens in the low  $\Delta K$  region but subsequently showed a reduction followed by an increase in  $da/dN$  in the high  $\Delta K$  region. The results for the top specimens present a higher level of scatter with a strong dependency on the specimen orientation. The FCG data for the specimens extracted from the top of the wall show an irregular wavy behavior in the vertical specimens (CT-T-1, CT-T-2, and CT-T-3), with at least one drop point, as depicted in Figure 4B, whereas the horizontal specimen (CT-T-4) exhibits a relatively straight crack growth trend in log-log axes. It can be seen in Figure 4B that in the vertical specimens, the FCG rates

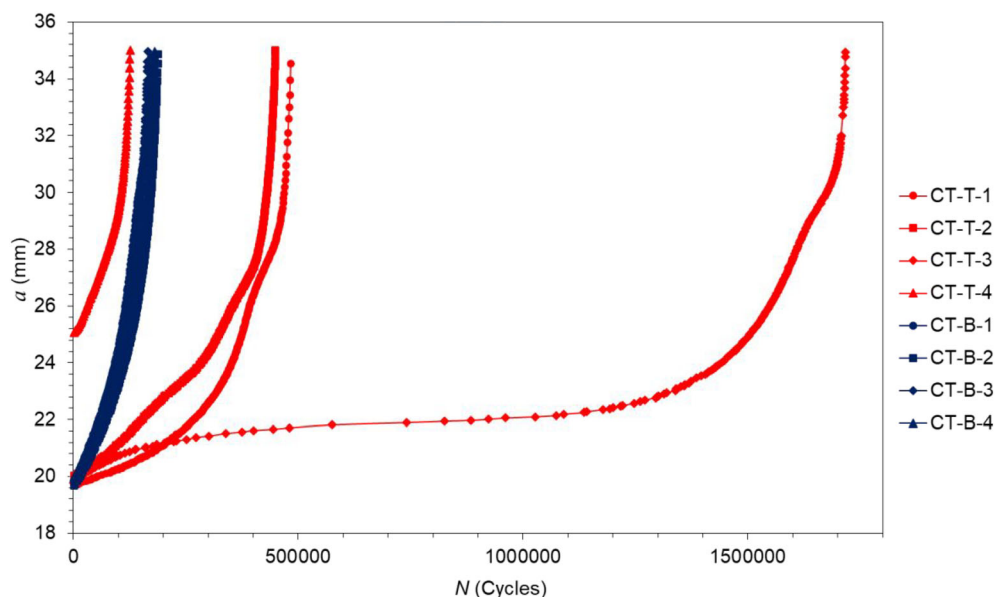
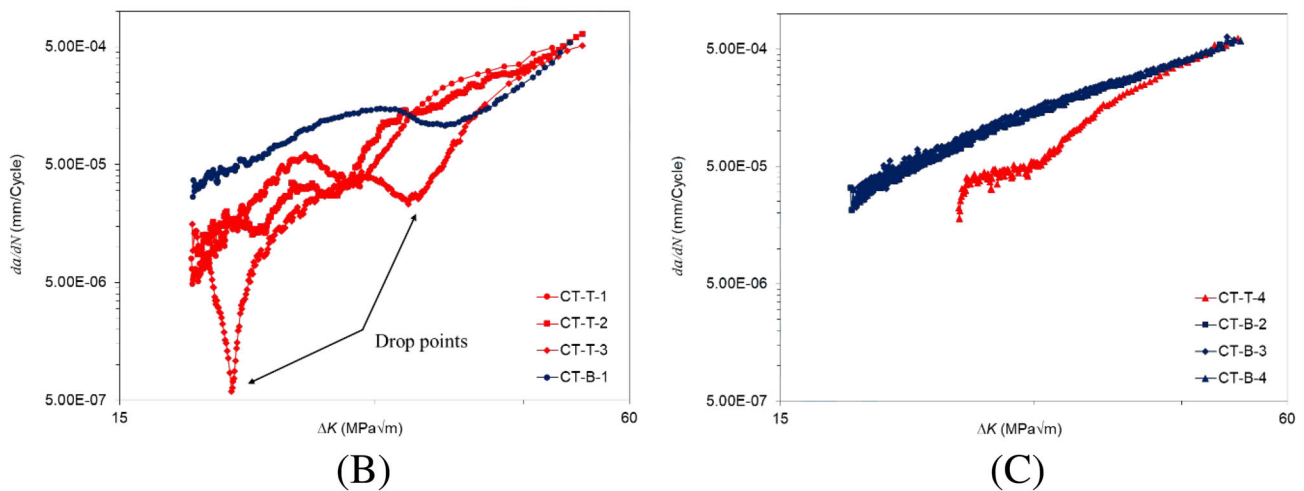
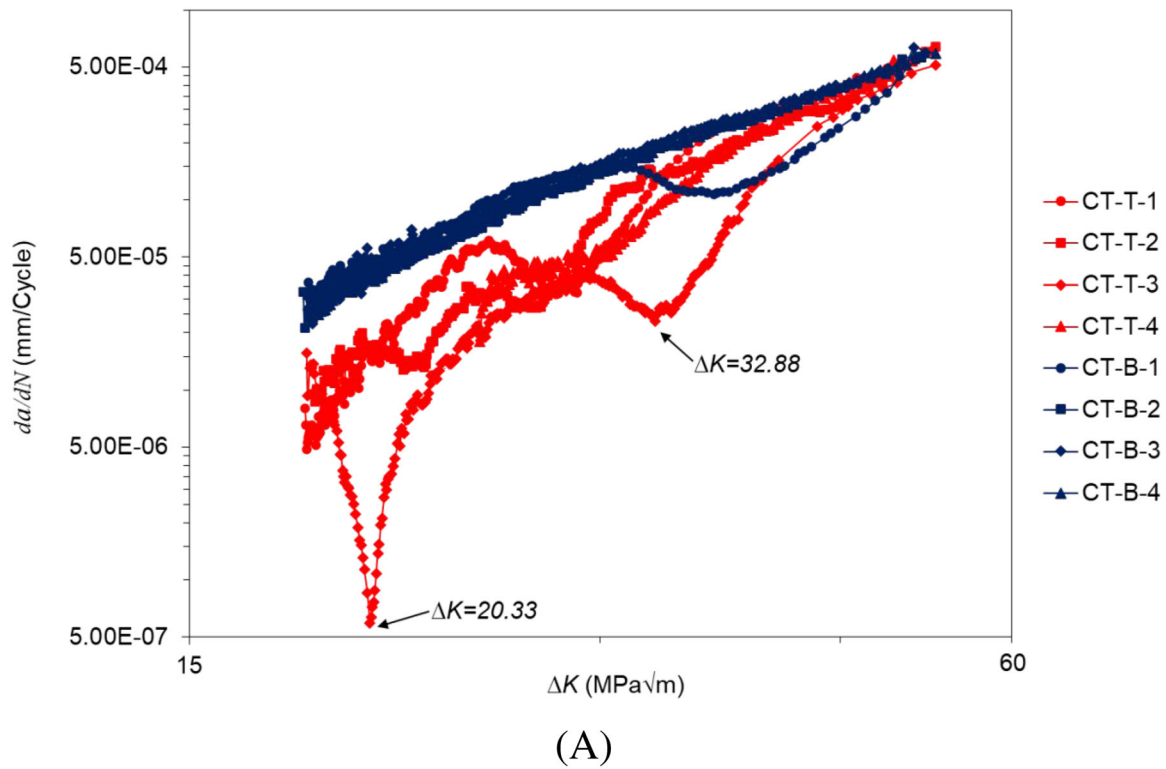


FIGURE 3 Fatigue crack growth trends in ER100S-1 WAAM built specimens extracted from different locations [Colour figure can be viewed at [wileyonlinelibrary.com](http://wileyonlinelibrary.com)]



**FIGURE 4** Fatigue crack growth rates results for ER100S-1 WAAM built specimens extracted from different locations: (A) all specimens, (B) vertical specimens, and (C) horizontal specimens [Colour figure can be viewed at [wileyonlinelibrary.com](http://wileyonlinelibrary.com)]

reduce by up to 17 times at the drop points while the horizontal specimens show a relatively smooth FCG behavior in specimens extracted both from the top and bottom of the wall (see Figure 4C). This can be due to the fact that in vertical specimens, the crack grows throughout different AM deposited layers; hence, the local material properties may vary which subsequently influence the FCG behavior of the material.

It is worth noting that the WAAM built wall was not subjected to any heat treatment. This was to replicate the realistic conditions where AM technology is used to

repair a damaged/cracked component and also in the case of large-scale, additively manufactured built structures, which cannot be heat treated in an oven due to their large size, and therefore high costs are involved in this process.<sup>29</sup> Although some residual stress profiles are expected to exist in the WAAM built wall before removing the base plate, the separation of the base plate from the additively manufactured wall followed by C(T) specimen extraction would significantly relax the initial residual stresses.<sup>30</sup> Therefore, it has been assumed in this study that the remaining residual stresses in extracted

C(T) specimens are insignificant and, as such, the applied loading condition has been employed in the analysis of the FCG behavior of the material. Further investigations will be conducted in future work to evaluate the influence of significant residual stress profiles on the subsequent fatigue behavior of large-scale WAAM built structures.

For all eight FCG datasets, the lines of best fit within the Paris region were plotted to work out the power law constants  $C$  and  $m$  (see Equation 2), which are summarized in Table 3. Additionally, the coefficient of determination,  $R^2$ , is included in the table for each dataset which has been found close to 1 for all horizontal specimens, indicating that the lines of best fit accurately describe the behavior of the material, and approximately 0.87 for vertical specimens due to the waviness of the obtained FCG curves. Typical values of the stress intensity factor range exponent,  $m$ , for FCG tests on wrought steel materials in air are within the range of 2 to 4<sup>31</sup>; however, only for three tested ER100S-1 WAAM specimens in this study has the  $m$  value been found within this range, and for the rest of the specimens, the  $m$  value is found to be between 4.10 and 5.56. Consequently, comparing the fatigue test results in Figure 4 and Table 3, it can be concluded that the extraction location (i.e., top and bottom) has a major impact on the  $da/dN$  vs.  $\Delta K$  trends of the ER100S-1 WAAM built specimens, whereas the orientation of the extracted specimens mostly affects the shape and level of scatter in the fatigue data.

$$\frac{da}{dN} = C \Delta K^m. \quad (2)$$

Subsequent to quantification of the Paris law constants for each of the tests performed in this study, the data were re-analyzed based on the specimen extraction location by plotting a line of best fit to all top and all bottom specimens, and the obtained results are summarized in Table 4. The results show that the value of  $R^2$  is higher for the specimens extracted from the bottom, Set-B, indicating less scatter in this dataset compared to the top specimens dataset, Set-T, which is consistent with observations previously made in Table 3. The level of scatter in the obtained FCG data was further analyzed by calculating the upper bound trends based on 2 standard deviation (SD), assuming the same slope as the mean line. The values of the power law constants for the upper bound FCG trends (mean + 2 SD) within the Paris region are reported in Table 4 for each dataset.

The mean + 2 SD FCG lines for the top (Set-T) and bottom (Set-B) specimen datasets are plotted in Figure 5 and compared with the recommended FCG trends in the BS7910 standard for welded joints, made of a wide range of wrought metals, in air, and based on the simplified law and two-stage law.<sup>32</sup> It can be seen in this figure that the upper bound lines for the Set-B and Set-T specimens extracted from the ER100S-1 WAAM built wall fall below the trends recommended in the BS7910 standard, indicating that the FCG behavior of ER100S-1 WAAM components can be conservatively predicted by the trends specified in the BS7910 standard. Moreover, it can be observed that the slope of the upper bound FCG line for Set-B is similar to the BS7910 2-stage law, while the slope of the Set-T upper

**TABLE 3** Paris law constants obtained from the tests performed on ER100S-1 WAAM built specimens ( $da/dN$  in mm/cycle and  $\Delta K$  in MPa  $\sqrt{m}$ )

Specimen ID	Orientation	Location	$P_{max}$ (kN)	$C$	$m$	$R^2$
CT-T-1	Vertical	Top	10	$4.08 \times 10^{-11}$	4.24	0.85
CT-T-2	Vertical	Top	10	$4.85 \times 10^{-11}$	4.17	0.96
CT-T-3	Vertical	Top	10	$1.52 \times 10^{-12}$	4.95	0.80
CT-T-4	Horizontal	Top	10	$3.20 \times 10^{-13}$	5.56	0.98
CT-B-1	Vertical	Bottom	10	$1.23 \times 10^{-7}$	1.99	0.86
CT-B-2	Horizontal	Bottom	10	$8.87 \times 10^{-10}$	3.63	0.99
CT-B-3	Horizontal	Bottom	10	$2.40 \times 10^{-10}$	4.10	0.99
CT-B-4	Horizontal	Bottom	10	$2.76 \times 10^{-9}$	3.27	0.99

**TABLE 4** Power law constants for the mean curves and upper bound trends in the Paris region for different specimen locations

Datasets	Location	$P_{max}$ (kN)	Mean			Mean + 2 SD	
			$C$	$m$	$R^2$	$C$	$m$
Set-B	Bottom	10	$1.00 \times 10^{-8}$	2.73	0.95	$1.69 \times 10^{-8}$	2.73
Set-T	Top	10	$3.00 \times 10^{-11}$	4.20	0.77	$1.05 \times 10^{-10}$	4.20

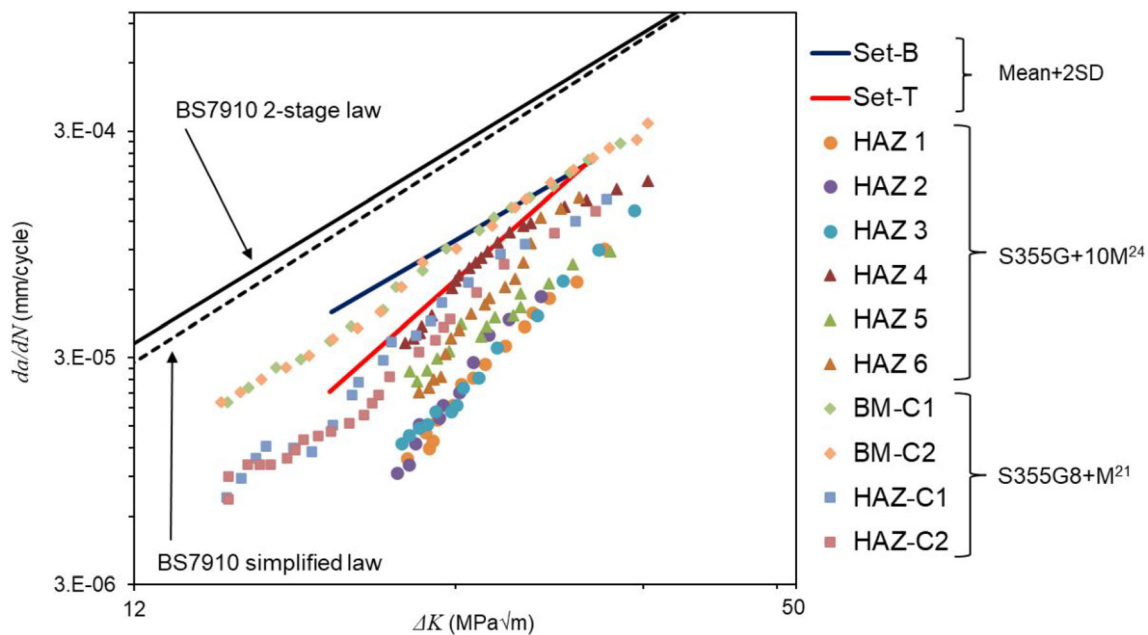


FIGURE 5 Comparison of the upper bound fatigue crack growth trends for ER100S-1 WAAM specimens with BS7910 curves and literature data on structural steels [Colour figure can be viewed at [wileyonlinelibrary.com](http://wileyonlinelibrary.com)]

bound line is much steeper than both trends recommended in the standard.

In addition to comparison of the results with BS7019 recommended trends, the FCG data obtained from this study were compared with the FCG data in air on wrought structural steels available in the literature. A set of C(T) specimens extracted from the heat affected zone (HAZ) for S355G + 10 M structural steel was tested by Jacob et al.<sup>33</sup> under similar loading conditions with  $P_{max} = 10$  kN, 5 Hz frequency, and  $R = 0.1$ . The same loading conditions were used to conduct the FCG test in air on S355G8 + M steel C(T) specimens extracted from HAZ and base metal (BM) by Mehmanparast et al.<sup>28</sup>. The results from these studies are presented in Figure 5 for comparison purposes and show that the upper bound FCG line for Set-B falls upon or above all the experimental data points obtained from S355G8 + M and S355G + 10 M steel BM and HAZ specimens. The slope of the set-T upper bound FCG line is similar to the experimental results from S355G + 10 M and S355G8 + M HAZ specimens. Both wrought steels taken for comparison are widely used for the fabrication of offshore structures that are subjected to severe cyclic loading conditions during their lifetime.<sup>34–36</sup> Hence, this comparison shows that ER100S-1 steel can be potentially considered for the WAAM fabrication of critical parts of offshore structures, demonstrating similar performance to the wrought steels currently used in conventional fabrication processes.

## 5 | MICROSTRUCTURAL ANALYSIS

### 5.1 | Fractography

After the FCG experiments were completed, all specimens were broken into halves for the post-mortem analysis in order to evaluate the accuracy of crack length estimation in fatigue tests using the compliance method. Prior to the break open, the specimens were soaked in liquid nitrogen for a few minutes to embrittle the material and then pulled under tension using the servo-hydraulic machine for fast fracture opening with minimum plastic deformation on the fracture surface. Two examples of the fracture surfaces are shown in Figure 6 for each of the top and bottom specimens extracted from the WAAM wall. Three areas are highlighted on the fracture surface of the FCG specimens in Figure 6: (1) pre-fatigue cracking, (2) fatigue crack growth, and (3) fast fracture. The crack extension in the first two regions was measured on all eight specimens. The fracture surface analysis reveals a symmetric crack propagation behavior with respect to the mid-thickness plane, indicating acceptable alignment in the test set-up during the FCG tests. Further examination of the fracture surfaces shows that the fatigue regions are smooth on the fracture surface of all specimens without any evidence of significant WAAM fabrication defects or any deviation of the crack from the straight plane. Moreover, it can be observed that the fracture surface of the vertical specimens

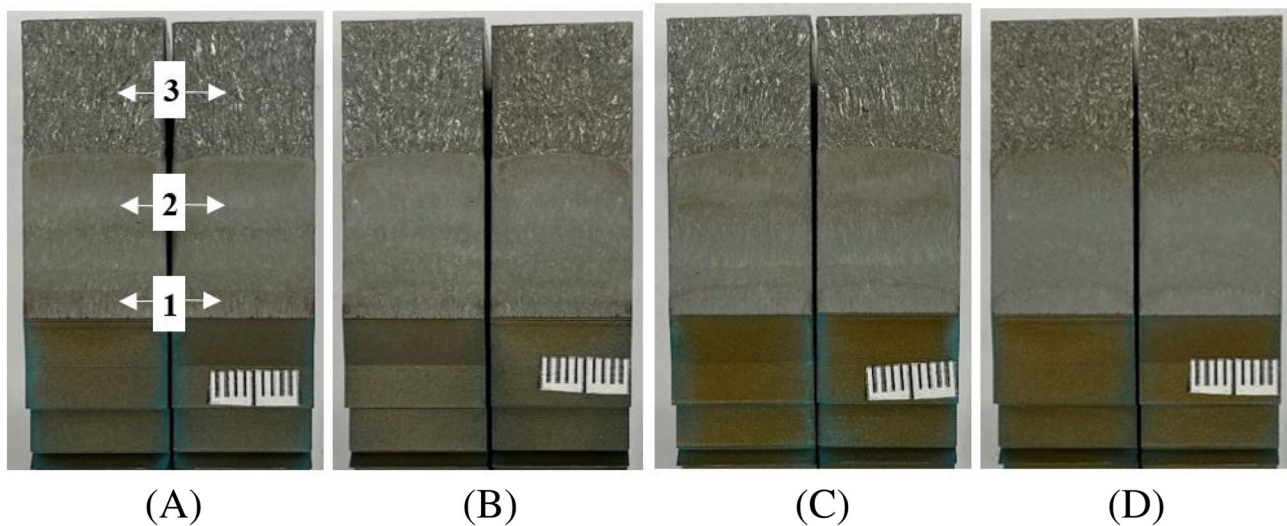


FIGURE 6 Fracture surface of WAAM built ER100S-1 specimens extracted from the top: (A) CT-T-1 and (B) CT-T-2, and from the bottom of the wall: (C) CT-B-1 and (D) CT-B-3 [Colour figure can be viewed at [wileyonlinelibrary.com](http://wileyonlinelibrary.com)]

TABLE 5 Specimen dimensions, initial, and final crack lengths

Specimen ID	$W$ (mm)	$B$ (mm)	$a_o$ (mm)	$a_{i,p}$ (mm)	$a_{f,c}$ (mm)	$a_{f,op}$ (mm)	% error in $a_f$
CT-T-1	50.1	16.0	17.0	19.7	35.0	35.5	1.3
CT-T-2	50.0	16.0	17.0	20.0	35.0	35.3	0.7
CT-T-3	50.0	16.1	17.0	19.8	35.0	35.4	1.2
CT-T-4	50.0	16.0	17.1	25.0	35.0	35.1	0.2
CT-B-1	50.1	16.0	17.0	19.8	35.0	35.3	0.8
CT-B-2	50.0	16.0	17.0	19.7	35.0	35.0	0.1
CT-B-3	50.0	16.2	17.1	19.8	35.0	34.7	0.8
CT-B-4	50.2	16.0	17.0	19.9	35.0	34.6	1.1

(Figure 6A–C) exhibited some waviness representing different AM layers of the WAAM wall, where the height of one layer was approximately 3 mm, whereas the fracture surface of the horizontal specimen (Figure 6D) is fairly flat, as the crack was propagating along a single AM layer. Additionally, the entire fracture surface of the vertical specimens, including the area of fast fracture, reveals a columnar texture with the lines perpendicular to the AM layers, and parallel to the WAAM deposition direction, which is absent on the horizontal specimen's fracture surface.

Some key specimen dimensions such as the machined crack length  $a_o$ , the crack length after the fatigue pre-cracking process (estimated from the compliance method)  $a_{i,p}$ , the final crack length after the FCG test (estimated from the compliance method)  $a_{f,c}$ , and the final crack length measured on the fracture surfaces (using optical imaging on the fracture surface)  $a_{f,op}$  are presented in Table 5. It can be seen in this table that the

percentage of error in the estimated crack lengths using the compliance method, in comparison with the measured crack lengths from optical imaging, is equal to or less than 1.3%. This implies that the compliance technique provides an accurate estimation of the crack length during the FCG experiments on WAAM built specimens.

## 5.2 | SEM analysis on fracture surface

Once all specimens were broken-open, the microscopy analysis was conducted on vertical specimens using a TESCAN VEGA 3 Scanning Electron Microscope (SEM), to examine the fracture surface areas of the vertical specimens corresponding to the FCG regions where the curve showed significant drops, such as areas A and C on the FCG curve for CT-T-3 in Figure 7. Area B between the two drop points was also selected to investigate any noticeable microstructural differences. Moreover, for

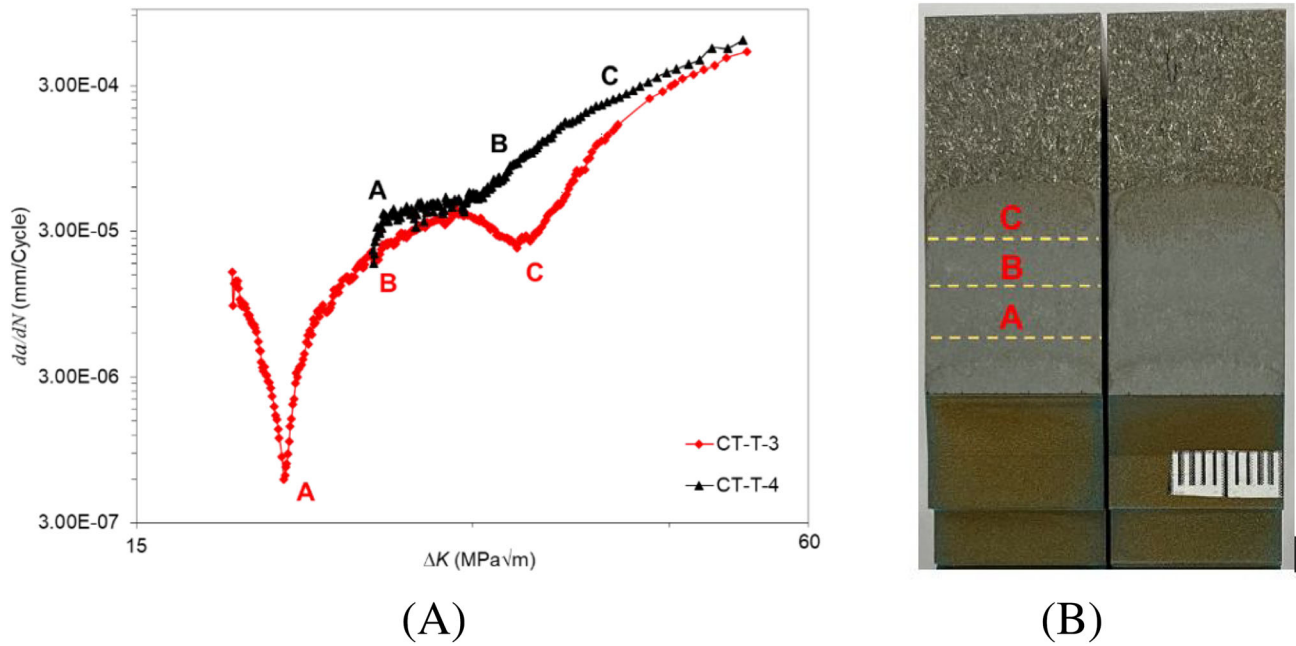


FIGURE 7 (A) Areas of interest for SEM analysis on vertical specimen CT-T-3 and horizontal specimen CT-T-4; (B) demonstration of the investigated areas on the fracture surface [Colour figure can be viewed at wileyonlinelibrary.com]

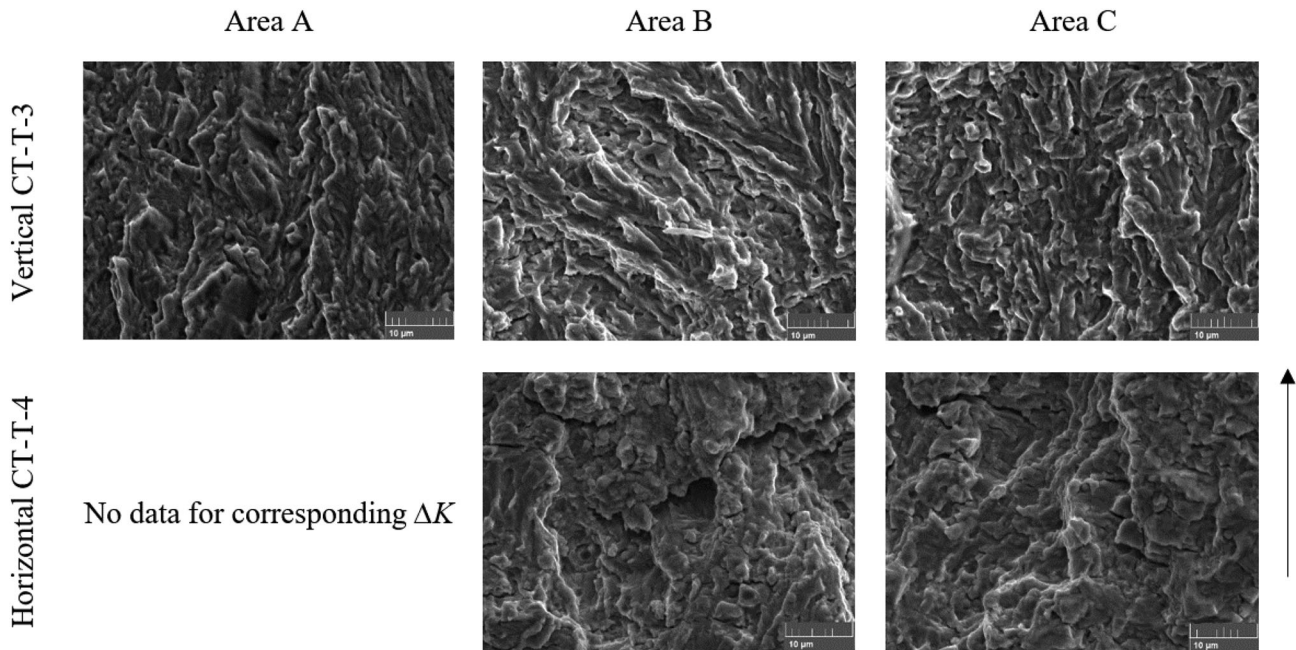


FIGURE 8 SEM fractographs of three areas on vertical (CT-T-3) and horizontal (CT-T-4) specimens with 5,000 magnification (the scale bar is 10 μm, and the right-hand side arrow shows the direction of the crack propagation)

comparison purposes, the fracture surface of a horizontal specimen, CT-T-4, extracted from the top of the WAAM wall was also examined. Since the obtained FCG trend of the horizontal specimen is relatively straight in log-log axes, areas of interest were selected with the same  $\Delta K$  values that correspond to the vertical specimen, as depicted in Figure 7A.

The SEM analysis of the three areas of interest for the horizontal and vertical specimens is shown in Figure 8, with a magnification of 5,000. Fracture surfaces of both vertical and horizontal specimens revealed transgranular cup and cone features, suggesting a ductile fracture mechanism. However, these ductile fracture features of the vertical specimen are smaller and with higher

density, while for the horizontal specimen, there are fewer of them and with a larger size. Additionally, the microstructural analysis of the fracture surface of the horizontal specimen CT-T-4 reveals the presence of large horizontal secondary cracks that lead to higher FCG rates, compared with the vertically oriented specimen CT-T-3, which is consistent with the FCG trends observed in Figure 7A. Furthermore, there are elongated dimples on the vertical specimen with different orientations, compared to the horizontal specimen. In areas A and C, where the drop of FCG rate is visible, the orientation of the dimples on vertical the CT-T-3 specimen is upwards and parallel to the crack propagation direction, whereas in area B, the orientation of rupture changes and inclines to approximately  $55^\circ$  with respect to the crack propagation direction, which accelerates the crack rate compared to areas A and C. These observations are consistent with the observed FCG trend seen in Figure 7A. The microstructural difference of areas A and C, along with the drop of the FCG rates, can happen when the crack tip is encountering the re-melted zone between two WAAM layers; however, to confirm this fact, further hardness mapping and microstructural investigation were conducted.

### 5.3 | Microhardness mapping

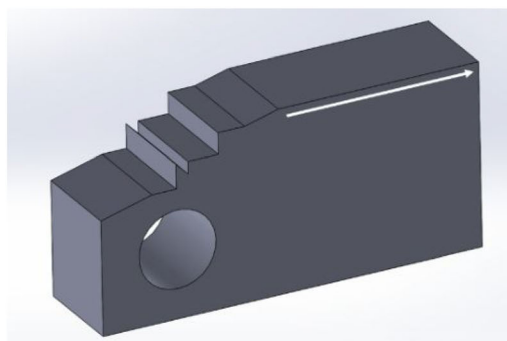
The same vertical specimen (CT-T-3) was taken for further microhardness analysis to examine how the hardness changes along the crack propagation path. As depicted in Figure 9A, hardness values were measured on the front face of the specimen from the initial crack tip location, towards the end of the specimen, with the same direction as the crack propagation path during FCG test, at approximately 0.2 mm from the edge of the specimen. Measurements were carried out according to BS EN

ISO 6507-1:1997<sup>37</sup> using a 0.5 kg load, in which the applied load was held for 15 s and the indentations were conducted at 2 mm intervals. The hardness results are presented in Figure 9B. The areas of interest were also marked in the figure and show that area A corresponds to the lowest hardness value of the tested plane (approximately 235 HV), whereas area C lays in the region with the highest hardness at about 258 HV; hardness value in area B is 248 HV. This confirms that the drops in the FCG rates do not depend on the microhardness of ER100S-1 material for WAAM components.

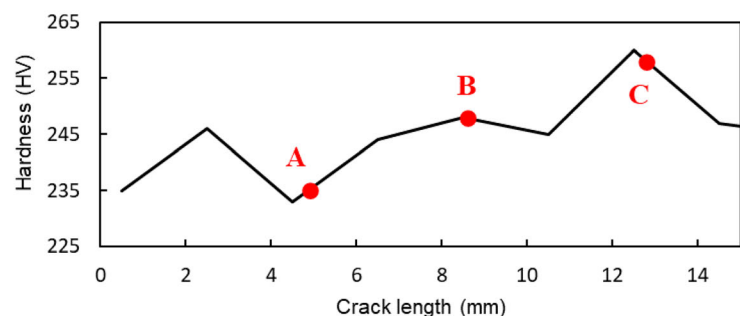
### 5.4 | Optical microscopy analysis

A thin slice of the fracture surface, which was approximately 1.5 mm thick, was cut off from the vertical specimen's fracture surface of CT-T-3 using the EDM technique. The sample was then hot-mounted in mold, ground (with final grinding step of 2,500 grit), polished using DiaPro Dac 3  $\mu\text{m}$  diamond suspension, final polished using OP-S colloidal silica suspension with a grain size of about 0.04  $\mu\text{m}$ , and then etched using 2% Nital solution in accordance with ASTM E407-07.<sup>38</sup> This etchant reveals alpha grain boundaries and constituents. The microstructures of the etched specimen were observed using a digital microscope HIROX, MXB-2500REZ, at the exact areas A,–C specified in Figure 7, and the results are presented in Figure 10.

The material microstructures in areas A and C in Figure 10 demonstrate that the crack is traveling between two WAAM layers, hence why a reduction in the FCG rate is observed at the  $\Delta K$  values corresponding to these regions. On the other hand, the microscopical analysis of area B shows a region with a single WAAM layer that does not affect the FCG behavior. Based on this analysis, it can be concluded that the specimen orientation plays a



(A)



(B)

FIGURE 9 (A) Microhardness mapping path and (B) hardness test results along the crack path for the vertical specimen CT-T-3 [Colour figure can be viewed at [wileyonlinelibrary.com](http://wileyonlinelibrary.com)]

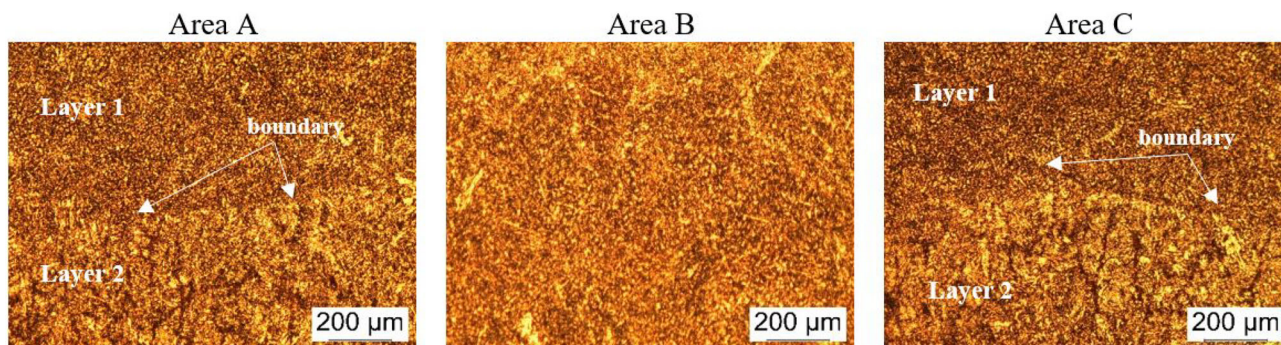


FIGURE 10 Optical microscopy analysis of vertical specimen CT-T-3 at three different areas of interest [Colour figure can be viewed at [wileyonlinelibrary.com](http://wileyonlinelibrary.com)]

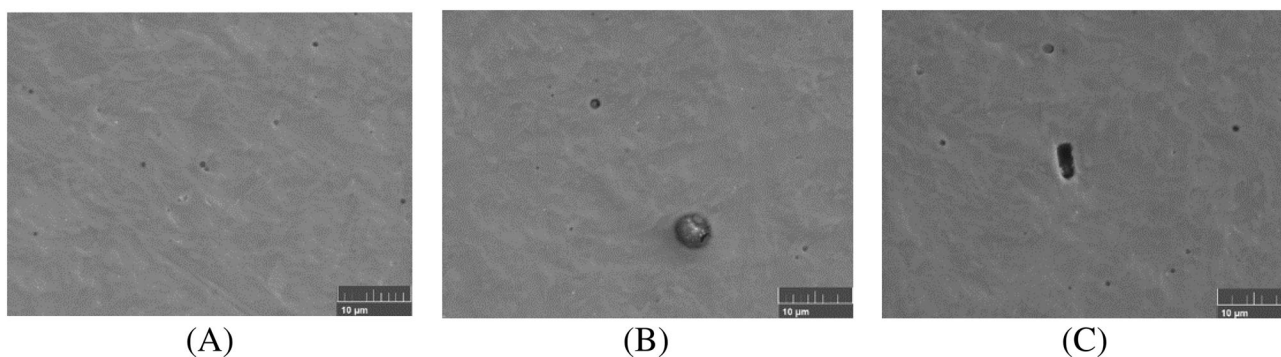


FIGURE 11 SEM fractographs of polished ER100S-1 specimens with defects (A) and (B) gas-entrapped pores and (C) pores and a keyhole porosity defect (the scale bar is 10 µm)

significant role in microstructural variations along the crack path and consequently the FCG behavior of WAAM ER100S-1 specimens. The microstructural observations also confirm that the vertical specimen orientation requires a higher amount of energy for a crack to propagate at the boundaries between two consecutive WAAM layers and exhibits a lower FCG rate in such regions, compared to the horizontal specimens where the crack propagates throughout only a single WAAM layer and does not require extra amounts of energy for crack propagation (Figure 7A).

## 5.5 | Defects

The WAAM technique is a continuous welding process. During the fabrication of WAAM components, the quality of the metal deposition depends on the process parameters (CMT power, layer thickness, deposition rate, etc.) and can be unstable due to complex mass and heat transfer, which leads to variety of defects, such as porosity, lack-of-fusion, distortion, or cracking.<sup>39,40</sup> The embedded defects or flaws can affect the mechanical behavior of the WAAM component and

significantly reduce its fatigue life.<sup>39</sup> Previous analysis of the fracture surfaces in Figure 6 did not indicate any visible defects at low magnifications; therefore, in order to examine the existence of potential defects in more detail, all polished specimens were inspected with an SEM, and some key observations are presented in Figure 11. As can be seen, porosity defects are observed in all three images, with the maximum diameter of approximately 5 µm. Moreover, a combination of a keyhole and gas-entrapped pores porosity defect is visible in Figure 11C. The typical pore size reported for WAAM built components in the literature varies from 10 to <100 µm<sup>41–43</sup>; therefore, due to the small size of the discovered defects, the manufactured ER100S-1 WAAM part produced for this study can be considered as a low level defects component.

## 6 | CONCLUSIONS

The FCG behavior of ER100S-1 WAAM built specimens was investigated in this study. Based on the observations and analysis of the collected data, the following conclusions can be drawn:

- The duration of the experiments on the C(T) specimens extracted from the top of the WAAM built walls is on average 3.9 times longer than for the bottom specimens.
- At the beginning of the Paris region, the specimens extracted from the top of the WAAM wall exhibit slower FCG rates; however, at higher  $\Delta K$  values, all specimens extracted from both top and bottom show similar trends.
- The specimen orientation affects the shape of the FCG trends and the level of scatter, with wavy FCG data patterns and high level of scatter observed in the vertical specimens.
- The mean + 2 SD FCG lines for both top and bottom sets of specimens fall below the recommended FCG trend in BS7910.
- The upper bound trend for set-B lies upon or above the FCG data points obtained from S355G8 + Mand S355G + 10 M BM and HAZ specimens, while the slope of the upper bound line for set-T aligns with S355G8 + M and S355G + 10 M HAZ specimens.
- The SEM analysis of fracture surfaces revealed the ductile fracture mechanism for both horizontal and vertical specimens. However, the presence of large secondary cracks perpendicular to the crack propagation direction in the horizontal specimens accelerates the FCG rate compared to the vertical specimens.
- Optical microscopy analysis demonstrated that the drops in FCG rates in vertical specimens occur when the crack propagates through the boundary between two consecutive WAAM layers.
- Examination of polished ER100S-1 WAAM specimens under SEM confirmed a low level of defects, with the maximum pore diameter of approximately 5  $\mu\text{m}$ .

## ACKNOWLEDGMENT

This work was supported by grant EP/L016303/1 for Cranfield, Oxford, and Strathclyde Universities' Centre for Doctoral Training in Renewable Energy Marine Structures – REMS CDT (<http://www.rems-cdt.ac.uk/>) from the UK Engineering and Physical Sciences Research Council (EPSRC).

## AUTHOR CONTRIBUTIONS

Anna Ermakova worked on methodology, planned and conducted all experiments, analysed the data and wrote the original draft of the paper. Ali Mehmanparast developed the concept and supervised the project, contributed to the interpretation of the results. Ali Mehmanparast, Supriyo Ganguly, Javad Razavi and Filippo Berto contributed to the final version of the manuscript.

## DATA AVAILABILITY STATEMENT

The data that support the findings of this study are available from the corresponding author upon reasonable request.

## NOMENCLATURE

$a_0$	initial crack length
$a_i$	instantaneous crack length
$a_{i,p}$	crack length after pre-fatigue cracking
$a_{f,c}$	final crack length estimated from the compliance data
$a_{f,op}$	final crack length measured from the fracture surface
$B$	total thickness
$C$	material dependent coefficient in the Paris law equation
$da/dN$	fatigue crack growth rate
$H$	specimen height
$K_{max}$	stress intensity factor at $P_{max}$
$\Delta K$	stress intensity factor range
$m$	material dependent exponent in the Paris law equation
$P_{max}$	maximum load in a fatigue cycle
$P_{min}$	minimum load in a fatigue cycle
$R$	load ratio
$W$	specimen width
AM	additive manufacturing
B	bottom
BM	base metal
C(T)	compact tension specimen
CMT	cold metal transfer
EDM	electrical discharge machining
FCG	fatigue crack growth
H	horizontal WAAM built C(T) specimens
SEM	scanning electron microscope
SEN(B)	single edge notched bend specimen
SIF	stress intensity factor
T	top
UTS	ultimate tensile strength
V	vertical WAAM built C(T) specimens
WAAM	wire arc additive manufacturing

## REFERENCES

1. Frazier WE. Metal additive manufacturing: a review. *J Mater Eng Perform.* 2014;23(6):1917-1928.
2. Selcuk C. Laser metal deposition for powder metallurgy parts. *Powder Metall.* 2011;54:94-99.
3. Berto F, Razavi SMJ, Torgersen J. Frontiers of fracture and fatigue: some recent applications of the local strain energy density. *Fratt Ed Integr Strutt.* 2018;12:1-32.
4. Martina F, Ding J, Williams S, Caballero A, Pardal G, Quintino L. Tandem metal inert gas process for high

- productivity wire arc additive manufacturing in stainless steel. *Addit Manuf.* 2019;25:545-550.
5. Marinelli G, Martina F, Lewtas H, Hancock D, Ganguly S, Williams S. Functionally graded structures of refractory metals by wire arc additive manufacturing. *Sci Technol Weld Join.* 2019;24(5):495-503.
  6. Balit Y, Joly LR, Szmytka F, Durbecq S, Charkaluk E, Constantinescu A. Self-heating behavior during cyclic loadings of 316L stainless steel specimens manufactured or repaired by Directed Energy Deposition. *Mater Sci Eng A.* 2020;786:139476.
  7. Li Y, Han Q, Horváth I, Zhang G. Repairing surface defects of metal parts by groove machining and wire + arc based filling. *J Mater Process Technol.* 2019;274:116268.
  8. Thapliyal S. Challenges associated with the wire arc additive manufacturing (WAAM) of aluminum alloys. *Mater Res Exp.* 2019;6(11):112006.
  9. Najmon JC, Raeisi S, Tovar A. Review of additive manufacturing technologies and applications in the aerospace industry. In: *Additive Manufacturing for the Aerospace Industry.* Elsevier Inc.; 2019:7-31.
  10. Gardner L, Kyvelou P, Herbert G, Buchanan C. Testing and initial verification of the world's first metal 3D printed bridge. *J Constr Steel Res.* 2020;172:106233.
  11. Mehmanparast A, Taylor J, Brennan F, Tavares I. Experimental investigation of mechanical and fracture properties of offshore wind monopile weldments: SLIC interlaboratory test results. *Fatigue Fract Eng Mater Struct.* 2018;41:2485-2501.
  12. Jacob A, Mehmanparast A, D'Urzo R, Kelleher J. Experimental and numerical investigation of residual stress effects on fatigue crack growth behaviour of S355 steel weldments. *Int J Fatigue.* 2019;128:105196.
  13. Anandavijayan S, Mehmanparast A, Braithwaite J, Brennan F, Chahardehi A. Material pre-straining effects on fatigue behaviour of S355 structural steel. *J Constr Steel Res.* 2021;183:106707.
  14. Zhang X, Martina F, Ding J, Wang X, Williams SW. Fracture toughness and fatigue crack growth rate properties in wire + arc additive manufactured Ti-6Al-4V. *Fatigue Fract Eng Mater Struct.* 2017;40:790-803.
  15. Zhang X, Martina F, Syed AK, Wang X, Ding J, Williams SW. Fatigue crack growth in additive manufactured titanium: residual stress control and life evaluation method development. *29th ICAF Symposium-Nagoya.* 2017:7-9.
  16. Smith TR, Sugar JD, Schoenung JM, San Marchi C. Relationship between manufacturing defects and fatigue properties of additive manufactured austenitic stainless steel. *Mater Sci Eng A.* 2019;765:138268.
  17. Gordon J, Hochhalter J, Haden C, Harlow DG. Enhancement in fatigue performance of metastable austenitic stainless steel through directed energy deposition additive manufacturing. *Mater Des.* 2019;168:107630.
  18. Zhang J, Wang X, Paddea S, Zhang X. Fatigue crack propagation behaviour in wire + arc additive manufactured Ti-6Al-4V: Effects of microstructure and residual stress. *Mater Des.* 2016; 90:551-561.
  19. Zhang J, Zhang X, Wang X, et al. Crack path selection at the interface of wrought and wire + arc additive manufactured Ti-6Al-4V. *Mater Des.* 2016;104:365-375.
  20. Gordon JV, Haden CV, Nied HF, Vinci RP, Harlow DG. Fatigue crack growth anisotropy, texture and residual stress in austenitic steel made by wire and arc additive manufacturing. *Mater Sci Eng A.* 2018;724:431-438.
  21. Zhang X, Martina F, Syed AK, Ding J. Fatigue crack growth in additive manufactured titanium: residual stress control and life evaluation method development. 2017:7-9.
  22. ER100S-1 Data Sheet. Pinnacle alloys. Washington D.C.
  23. ER100S-G Data Sheet Böhler welding. 2014.
  24. Ermakova A, Mehmanparast A, Ganguly S. A review of present status and challenges of using additive manufacturing technology for offshore wind applications. *Procedia Struct Integr.* 2019; 17:29-36.
  25. ASTM E647-13. Standard test method for measurement of fatigue crack growth rates. *American Society for Testing and Materials.* 2014:1-50.
  26. American Society for Testing and Materials. ASTM E1820-11: standard test method for measurement of fracture toughness. *Annual book of ASTM standards.* 2011:1-55.
  27. Ermakova A, Mehmanparast A, Ganguly S, Razavi J, Berto F. Investigation of mechanical and fracture properties of wire and arc additively manufactured low carbon steel components. *Theor Appl Fract Mech.* 2020;109:102685.
  28. Mehmanparast A, Brennan F, Tavares I. Fatigue crack growth rates for offshore wind monopile weldments in air and seawater: SLIC inter-laboratory test results. *Mater Des.* 2017;114: 494-504.
  29. Wang Z, Stoica AD, Ma D, Beese AM. Stress relaxation behavior and mechanisms in Ti-6Al-4V determined via in situ neutron diffraction: application to additive manufacturing. *Mater Sci Eng A.* 2017;707:585-592.
  30. Hönnige JR, Colegrove PA, Ahmad B, et al. Residual stress and texture control in Ti-6Al-4V wire + arc additively manufactured intersections by stress relief and rolling. *Mater Des.* 2018;150:193-205.
  31. Anderson TL. *Fracture Mechanics: Fundamentals and Application.* 3rd ed. Boca Raton: Taylor & Francis Group; 2005.
  32. BS 7910. BSI Standards Publication Guide to methods for assessing the acceptability of flaws in metallic structures. *BSI Standards Publication.* 2015:490.
  33. Jacob A, Oliveira J, Mehmanparast A, Hosseinzadeh F, Kelleher J, Berto F. Residual stress measurements in offshore wind monopile weldments using neutron diffraction technique and contour method. *Theor Appl Fract Mech.* 2018;96: 418-427.
  34. Adedipe O, Brennan F, Kolios A. Review of corrosion fatigue in offshore structures: present status and challenges in the offshore wind sector. *Renew Sustain Energy Rev.* 2016;61: 141-154.
  35. Lotsberg I, Sigurdsson G, Fjeldstad A, Moan T. Probabilistic methods for planning of inspection for fatigue cracks in offshore structures. *Mar Struct.* 2016;46:167-192.
  36. Jacob A, Mehmanparast A. Crack growth direction effects on corrosion-fatigue behaviour of offshore wind turbine steel weldments. *Mar Struct.* 2021;75:102881.
  37. International Standard ISO. Metallic materials—Vickers hardness test—part 1: test method (ISO 6507-1: 2018). International Standard 2018:1-49.

38. Practice S. Standard practice for microetching metals and alloys ASTM E-407. 2016;7:1-22.
39. Wu B, Pan Z, Ding D, et al. A review of the wire arc additive manufacturing of metals: properties, defects and quality improvement. *J Manuf Process*. 2018;35:127-139.
40. Javadi Y, MacLeod CN, Pierce SG, et al. Ultrasonic phased array inspection of a Wire + Arc Additive Manufactured (WAAM) sample with intentionally embedded defects. *Addit Manuf*. 2019;29:100806.
41. Derekar KS. A review of wire arc additive manufacturing and advances in wire arc additive manufacturing of aluminium. *Mater Sci Technol (United Kingdom)*. 2018;34:895-916.
42. Al-Nabulsi Z, Mottram JT, Gillie M, Kourra N, Williams MA. Mechanical and X ray computed tomography characterisation of a WAAM 3D printed steel plate for structural engineering applications. *Construct Build Mater*. 2021;274:121700.
43. Xiong J, Zhang G, Zhang W. Forming appearance analysis in multi-layer single-pass GMAW-based additive manufacturing. *Int J Adv Manuf Technol*. 2015;80(9-12):1767-1776.

**How to cite this article:** Ermakova A, Ganguly S, Razavi J, Berto F, Mehmanparast A. Experimental investigation of the fatigue crack growth behavior in wire arc additively manufactured ER100S-1 steel specimens. *Fatigue Fract Eng Mater Struct*. 2021; 1-15. doi:10.1111/ffe.13598